1-1-2003

A Fixed-Grid Front-Tracking Algorithm for Solidification Problems. Part II - Directional Solidification with Melt Convection

C. Y. Li

S V. Garimella
Purdue University, sureshg@purdue.edu

J E. Simpson

Li, C. Y.; Garimella, S V.; and Simpson, J E., "A Fixed-Grid Front-Tracking Algorithm for Solidification Problems. Part II - Directional Solidification with Melt Convection" (2003). *CTRC Research Publications.* Paper 78.
http://dx.doi.org/10.1080/10407790390121970

A Fixed-Grid Front-Tracking Algorithm for Solidification Problems. Part II – Directional Solidification with Melt Convection[¶]

Chin-Yuan Li[§], **Suresh V. Garimella**[†] and **James E. Simpson**[‡]
School of Mechanical Engineering
Purdue University
West Lafayette, Indiana 47907-1288

Phone: (765) 494-5621 Fax: (765) 494-0539
Email: sureshg@ecn.purdue.edu

ABSTRACT

A numerical study of directional solidification has been performed using a fixed-grid front-tracking algorithm. The directional solidification of pure tin, as well as the horizontal Bridgman growth of pure succinonitrile, were investigated. In both cases, the growth front was stable and non-dendritic, but was significantly distorted by the influence of convection in the melt and, for the Bridgman growth case, by the translation of temperatures at the boundaries which represents furnace movement. Results obtained for the directional solidification of pure tin were found to agree reasonably well with experimental and numerical data for temperatures and front locations obtained from the literature. For the Bridgman growth of succinonitrile, the results were compared with detailed experimental data obtained from carefully controlled experiments, and numerical simulations reported in the literature. The predicted interface shapes and melt velocities agree well with experimental results. The predicted front locations exhibit superior agreement to the experimental data than those obtained in the literature using other numerical techniques.

¶ Submitted for publication in *Numerical Heat Transfer*, August 2002

§ Graduate Student

† Professor, ***person to whom correspondence should be addressed***

‡ Postdoctoral Research Associate

INTRODUCTION

High-performance materials used in aerospace, military and electronics applications require low levels of defects and high levels of solute uniformity. Directional solidification (Fig. 1a) is a highly controlled process that can be employed to synthesize such high-quality materials. In directional solidification, heat is extracted from the mold primarily in one direction, and the crystal grows aligned and opposed to the direction of heat extraction. By controlling the rate of heat extraction and the melt superheat, the crystal growth rate can be controlled and the interface can be kept planar rather than dendritic. During directional solidification, heat and mass transfer by both diffusion and convection driven by thermal and solutal gradients influence the shape of this solid/liquid interface and hence the dopant segregation levels, thus directly determining the final crystal quality [1].

Bridgman crystal growth is one of the directional solidification processes used in industry to produce high quality materials [2]. A schematic of this process is shown in Fig. 1(b). The furnaces used in the Bridgman growth process results in the existence of a high-temperature zone where the temperature is above the melting point of the crystal, a low-temperature zone, and an adiabatic zone between the two. Initially, the ampoule containing the charge is moved into the high-temperature zone until only the single crystal seed remains unmelted in the low-temperature zone. Later, the ampoule is pulled slowly toward the low-temperature zone to initiate crystal growth. Key process parameters include the applied furnace temperature distribution and rate of translation, ampoule properties and furnace orientation.

Experimental investigations of solidification processes which involve metallic melts are complicated by the opacity, reactivity and high temperatures of the melts. Accurate experimental determination of the interface shape and convection is difficult. As a result, solidification

experiments have often been performed with transparent materials that solidify in a manner analogous to metals [3-9].

In the present study, numerical simulations were first performed of the directional solidification of pure tin, using a new fixed-grid front-tracking algorithm [10, 11]. The model results for interface shapes and temperatures were compared to experimental data from the literature [12] as well as simulated data generated using other algorithms [13-15]. It was found that the results compared reasonably well with the experimental and numerical data. Next, simulations of the Bridgman growth of pure succinonitrile (SCN) were performed, under both no-growth and growth conditions. Again, the results from the numerical solution scheme were compared with experimental and numerical data from the literature [16]. The experimental data in [16] were obtained under carefully controlled conditions with a view to benchmarking numerical simulation techniques, and included melt velocity data. It was found that the results produced with the front-tracking algorithm agreed well with the experimental data, and were able to more accurately represent the front location than the numerical simulations reported in the literature, which did not explicity track the front. Finally, the numerical results provide valuable insight into the role of convection in directional solidification processes.

GOVERNING EQUATIONS

The problems under consideration are the directional solidification of pure tin (Fig. 1a) and the Bridgman growth of pure succinonitrile (Fig. 1b). Thermophysical properties are assumed to be constant but distinct for each phase. In the melt region, the flow is driven by buoyancy-induced natural convection and is considered incompressible. The governing equations for mass and momentum conservation in the liquid phase are the *continuity* and *Navier-Stokes* equations:

$$\tilde{\nabla} \cdot \tilde{U} = 0 \tag{1}$$

$$\frac{\partial \tilde{U}}{\partial t} + \tilde{U} \cdot \tilde{\nabla} \tilde{U} = -\frac{\tilde{\nabla} P}{\rho} + \upsilon \nabla^2 \tilde{U} - \tilde{g} \beta_T (T - T_0) \tag{2}$$

In Eq. (2) the final term is the Boussinesq approximation for the creation of momentum from density changes due to thermal gradients. For the present work, the reference temperature T_0 is taken to be the melting temperature. The governing equation for conservation of energy is:

$$\left(\frac{\partial T_i}{\partial t} + \tilde{U} \cdot \tilde{\nabla} T_i \right) = \tilde{\nabla} \cdot (\alpha_i \tilde{\nabla} T) \qquad i = l, s \tag{3}$$

In the solid phase, velocities are zero throughout and there is no energy transport by convection.

The initial condition for momentum transport (Eq. 2) is that the fluid is quiescent:

$$\tilde{U} = 0 \tag{4}$$

The boundary condition at a plane, impermeable wall is the no-slip/no-penetration condition. The velocity is zero, as are the tangential derivatives of its components:

$$\begin{aligned} &\tilde{U} = 0 \\ &\frac{\partial (\tilde{U} \cdot \hat{\tau})}{\partial \tau} = 0 \end{aligned} \tag{5}$$

This relation holds true for both the moving solid/liquid interface and the walls of the domain.

The initial and boundary conditions imposed on the energy equation (Eq. 3) for the directional solidification of tin and the Bridgman growth of succinonitrile are complex and best understood by reference to Fig. 1. The condition at the solid/liquid interface that relates the release of latent heat at the interface to the interface velocity is the *Stefan condition* [1, 2]:

$$k_S \frac{\partial T_S}{\partial n} - k_L \frac{\partial T_L}{\partial n} = \Delta H V_n \tag{6}$$

The solution scheme required to solve these governing equations and the initial and boundary conditions for phase-change in directional solidification are described in the following section.

METHOD OF ANALYSIS

Front Tracking and Solution of Governing Equations

The fixed-grid front-tracking method used in the present study has been developed specifically to solve multidimensional phase-change problems. Full details of the scheme are given in Part I of this work [11] and are not repeated here. The process of interface tracking is accomplished in three steps: identification of marker points; calculation of surface normals; and identification of intersection points. Given a normal velocity, the marker points representing the interface can be advected to the next time step, and the interface reconstructed. However, the normal velocities are not known *a priori* in most problems of practical interest. Governing equations need to be solved in order to determine these velocities.

For the solution of the mass, momentum and energy equations, the spatial domain is discretized using a control volume approach. Fully implicit time discretization is used. The equations are solved using an adaptation of the SIMPLE algorithm [17, 18] with a staggered grid used for pressure correction. Many modifications to the discrete equations are required to handle the presence of the moving solid/liquid interface. These modifications are described in detail in this section.

Consider the general conservation equation:

$$\frac{\partial \Phi}{\partial t} + \tilde{U} \cdot \nabla \Phi = \Gamma \nabla^2 \Phi \tag{7}$$

For a regular control volume not containing the interface, the convective fluxes become

$$\sum_{nb}\left(\tilde{U}_{nb}\Phi_{nb}\right)d\hat{l}_{nb} = u_e\Phi_e l_e - u_w\Phi_w l_w + v_n\Phi_n l_n - v_s\Phi_s l_s \tag{8a}$$

in which

$$\Phi_e = \frac{\Phi_E + \Phi_P}{2}, \quad \Phi_w = \frac{\Phi_W + \Phi_P}{2}, \quad \Phi_n = \frac{\Phi_N + \Phi_P}{2}, \quad \Phi_s = \frac{\Phi_S + \Phi_P}{2} \tag{8b}$$

Thus, Eq. (8) becomes

$$\sum_{nb}\left(\tilde{U}_{nb}\Phi_{nb}\right)d\hat{l}_{nb} = B_E\Phi_E - B_W\Phi_W + B_N\Phi_N - B_S\Phi_S + B_P\Phi_P \tag{9}$$

where $B_{nb} = \frac{\tilde{U}_{nb}\hat{l}_{nb}}{2}$, *and* $B_P = B_E - B_W + B_N - B_S$. For a regular control volume not containing the interface, the diffusive fluxes become

$$\sum_{nb}\left(\Gamma\left(\frac{\partial\Phi}{\partial n}\right)\right)_{nb}^{n+1} d\hat{l}_{nb} = D_E\Phi_E + D_W\Phi_W + D_N\Phi_N + D_S\Phi_S - D_P\Phi_P \tag{10}$$

in which $D_{E,W,N.S} = \frac{(\Gamma l)_{E,W,N,S}}{\Delta h}$, $D_P = \left(D_E + D_W + D_N + D_S\right)$. The final discretized analog of the general conservation equation can therefore be written as:

$$\begin{aligned}&\frac{\Phi_P^{n+1} - \Phi_P^n}{dt}A_{cv} + B_E\Phi_E^{n+1} - B_W\Phi_W^{n+1} + B_N\Phi_N^{n+1} - B_S\Phi_S^{n+1} + B_P\Phi_P^{n+1}\\ &= D_E\Phi_E^{n+1} + D_W\Phi_W^{n+1} + D_N\Phi_N^{n+1} + D_S\Phi_S^{n+1} - D_P\Phi_P^{n+1} + \bar{S}\end{aligned} \tag{11}$$

Multiplying by $\frac{dt}{A_{cv}}$, we get:

$$\begin{aligned}\left(D_P^* + B_P^* + 1\right)\Phi_p^{n+1} = &\left(D_E^* - B_E^*\right)\Phi_E^{n+1} + \left(D_W^* + B_W^*\right)\Phi_W^{n+1}\\ &+ \left(D_N^* - B_N^*\right)\Phi_N^{n+1} + \left(D_S^* + B_S^*\right)\Phi_S^{n+1} + \bar{S}_P^* + \Phi_P^n\end{aligned} \tag{12}$$

The SIMPLE algorithm (used to solve for velocities) is essentially a guess-and-correct procedure for the calculation of pressure by defining the correction P' as the difference between the correct pressure field P and the guessed pressure field P^*. Detailed procedures for obtaining the equation for pressure correction are described in [17]. The discrete pressure correction equation for a regular cell can be written as:

$$a_{I,J}\, p'_{I,J} = a_{I+1,J}\, p'_{I+1,J} + a_{I-1,J}\, p'_{I-1,J} + a_{I,J+1} p'_{I,J+1} + a_{I,J-1} p'_{I,J-1} + b'_{I,J} \tag{13}$$

where $a_{I,J} = a_{I+1,J} + a_{I-1,J} + a_{I,J+1} + a_{I,J-1}$ and the coefficients are listed in Table 1.

Cells that contain the interface

"Cut" cells need treatment that is different from regular cells. A schematic in two dimensions is shown in Fig. 2(a). The enlarged figure shows the relationship of the marker point, intersection point, and control point with the grid lines. Two different cases can be identified. In Fig. 2(b), case A shows a situation where the distance between the marker point and grid point in the liquid is less than half of the grid length. This means that α, the distance between the marker point and the closest grid point along the vertical grid line in the solid phase, is greater than 0.5 ($\alpha_{A,I}$ in Fig. 2b). The control volume of the cut cell, as shown by the area with vertical shading, is smaller than one regular cell but greater than half of a regular cell in most cases. The other situation is case B shown in the same figure, where the cut cell, shaded with oblique lines, is bigger than a regular cell. The two cases can be distinguished by using the ratio (α) of the distance between the interface and the closest grid point in the *solid* phase along a vertical grid line and the grid size. This ratio α is larger than 0.5 for case A ($\alpha_{A,I}$), and smaller than 0.5 for case B ($\alpha_{B,I}$).

For a cut cell (I,J) as shown in Fig. 3(a) (case A), the discrete form for convective transport (Eq. 9) could be rewritten as

$$\sum_{nb}\left(U_{nb}\Phi_{nb}\right)\cdot d\hat{l}_{nb} = u_e\Phi_e l_e - u_w\Phi_w l_w + v_n\Phi_n l_n - v_I\Phi_{Iv} l_{Iv} + u_I\Phi_{Iu} l_{Iu} \tag{14}$$

where l_e is section CD, l_w is section AB, l_n is section BC and l_{Iv} and l_{Iu} are sections DF and AF, respectively. Φ_{nb} are all variables on the faces of the control cell, which need to be calculated by using the averaged values of two control points. For the values of Φ_e and Φ_{Ii}, however, linear interpoation between Φ_I and Φ_{ip} is used. We can rewrite Eq. (14) as

$$\sum_{nb}\left(U_{nb}\Phi_{nb}\right)\cdot d\hat{l}_{nb} = B_{ip}\Phi_{ip} - B_W\Phi_W + B_N\Phi_N - B_I\Phi_I + B_P\Phi_P \tag{15}$$

where B_W and B_N remain the same as in Eq. (9), but B_{ip} and B_I are substituted for the coefficients B_E and B_S.

In the same cut cell shown in Fig. 3(a), the diffusion coefficients for the discretized equation need to be redefined as well. Equation (10) is rewritten for the cut control cell (I,J) as

$$\begin{aligned}\oint_l \left(\Gamma\nabla\Phi\right)\cdot\hat{n}dl &= \sum_{nb}\left(\Gamma\left(\frac{\partial\Phi}{\partial n}\right)\right)_{nb}^{n+1} d\hat{l}_{nb} \\ &= \Gamma_e\left(\frac{\partial\Phi}{\partial x}\right)_e l_e - \Gamma_w\left(\frac{\partial\Phi}{\partial x}\right)_w l_w + \Gamma_n\left(\frac{\partial\Phi}{\partial y}\right)_n l_n - \Gamma_I\left(\frac{\partial\Phi}{\partial n}\right)_I l_I\end{aligned} \tag{16}$$

which can be written as

$$\sum_{nb}\left(\Gamma\left(\frac{\partial\Phi}{\partial n}\right)\right)_{nb}^{n+1} d\hat{l}_{nb} = D_{ip}\Phi_{ip} + D_W\Phi_W + D_N\Phi_N + D_I\Phi_I - D_P\Phi_P \tag{17}$$

The lengths along the control surfaces are as described previously. The fluxes through the surfaces of the control cell are still differenced using CDS for the west and north faces, but the other two faces are only differenced to first-order accuracy. Consequently, coefficients D_{ip}, D_I and D_P in Eq. (17) are different from those in Eq. (10).

Applying the pressure correction Eq. (13) to an irregular domain, new coefficients may be derived as shown in Table 2. The control volume for the cut cell is shown in Fig. 3(b). The contiunity equation is expressed in discrete form for this control volume ABCD:

$$\left[\left(\rho U_{i.J}\right)\cdot\overline{CD}\right]-\left[\left(\rho U_{i-1,J}\right)\cdot\overline{AB}\right]+\left[\left(\rho V_{I,j}\right)\cdot\overline{BC}\right]-\left[\left(\rho V_{I}\right)\cdot\overline{AD}\right]=0 \tag{18}$$

Since there is no velocity on the interface, the last term on the left hand side in Eq. (18) is zero. Upon substitution of the corrected velocities into the discretized continuity Eq. (18), it can be rearranged into the same form as Eq. (13) but with different coefficients. The modified coefficients are listed in Table 2.

Summary of Solution Scheme

A summary of the solution scheme is as follows:

1. Define marker points and intersection points and calculate the normal vector.
2. Calculate the normal velocities at each marker point.
3. Advect the marker points; the new locations of these points need not lie on the grid.
4. Obtain new marker points from the advected points, and calculate the surface normals.
5. Solve the governing equations in both phases, using the SIMPLE algorithm for velocities in the liquid phase as follows:
   a) Use prior pressure and temperature fields to solve the momentum equations in the liquid phase.
   b) Input the new velocities into the pressure correction equation to update the velocity and pressure fields which satisfy mass conservation.
   c) Use the updated velocity field to correct the temperature to satisfy the energy equation.
   d) Go to step (a), and repeat until temperature and velocity converge.

e) Go to step 3, and repeat the process for the next time step.

RESULTS AND DISCUSSION

Unidirectional Solidification of Pure Tin

The first problem considered involves the directional solidification of pure tin at a vertical wall in the presence of liquid superheat. The problem domain, and the initial and boundary conditions are shown in Fig. 1a. Since the present front tracking scheme must always consider the existence of a solid/liquid interface, a small part of the domain (thickness = 0.04 L) on the right hand side was considered to be solid and at the melting temperature at the start of the simulation. Since the solidification velocity is very fast in the beginning, the error from the difference of the initial condition may be neglected while comparing with experimental and other numerical results.

The important thermophysical properties for this case are shown in Table 3 and the other parameters are L = 8.89 cm, T_H = 233°C, T_C = 229°C, Pr = 0.017, and Ra = 1.4×10^5. The thermal properties for the liquid phase are considered to be different from those in the solid phase. Before choosing the appropriate mesh spacings and time step size for the simulations, a comprehensive grid-independence study was performed [as suggested in 14]. This study involved evaluating the solution fields of a test matrix of simulations at four different mesh spacings (Table 4) and four time-step sizes (Table 5) at two different finish times. The quantities examined were:

- u_{max}, the maximum magnitude of the horizontal velocity component, and its location
- v_{max} , the maximum magnitude of the vertical velocity component, and its location
- θ_{mid}, the value of nondimensional temperature at the midpoint of the solution domain (0.5, 0.375)
- x_f, the average value of the front location

In the tables, the percentages quoted are a comparison with the result at the last step of refinement.

The results indicate that a spatial discretization of 61 × 46 mesh points (grid size h =

0.01667), and a time step of $\Delta t = 1.25 \times 10^{-5}$ are the appropriate values, and these are applied throughout the simulation shown in this section. This grid size is similar to that used by other researchers who have simulated this problem using single-domain enthalpy-based methods [13, 14] or a coordinate-transforming scheme that explicitly tracks the interface [15].

Isotherms and velocity vectors at time $t = 0.165$ h for this simulation are shown in Fig. 4(a). By this time, the solidification front has propagated from the chilled wall through the cavity under the action of both conductive and convective heat transfer. As noted in [14], the isotherms in the solid region are typical of conduction in a solid; the temperature gradient is very steep because of pure conduction only. The isotherms become vertical as they approach the cold wall. In the liquid domain, the isotherms exhibit a distinct reverse "s" shaped distortion, which is characteristic of buoyancy-driven natural convection at a high Rayleigh number [21]. The isotherms compare well with the numerical results of [13] and [14]. The velocity vectors indicate that a strong convective cell has developed with almost quiescent fluid at the four corners of the liquid domain. Hot fluid rises at the hot (left) wall and flows along the top of the cell toward the solidification front, where it is cooled and falls to the lower surface under the action of gravity, circulating once again to the foot of the hot wall. This continual convection of warm fluid to the uppermost segment of the solidification front delays its propagation into the cavity. As a result, the solidification front is distorted into an "s"-shape (more perceptible at the later times in Figs. 4b and 4c) like the fluid isotherms. In the absence of buoyancy-induced natural convection, the solidification front would have been vertical [22].

Figure 4(b) shows velocity vectors and isotherms at a later time in the simulation, $t = 0.529$ h. The results compare well with those reported in [14, 15]. Results further into the solidification process are shown in Fig. 4(c) for time $t = 1.896$ h. The solidification front has propagated much

further into the melt, with over half of the cavity being comprised of solid tin. The velocity vectors show a single convective cell covering most of the melt domain, as in [13].

Nondimensional temperatures Θ (defined in the nomenclature) are shown along three different cavity heights in Fig. 5(a) at time t = 0.077 h. Corresponding experimental values from [12] and predictions from [13, 14] are also shown. The curves for y/H = 0.9 and y/H = 0.5 indicate reasonable agreement with the experimental data. Thermal inertia of the test apparatus is a possible cause for the discrepancies noted. The experimental apparatus was not capable of producing an instantaneous temperature drop to T_C at the cold wall at time t = 0; rather 0.033 h elapsed before the cold plate temperature reached T_C [12]. The curve for y/H = 0.1 is significantly different from the experimental results, with the numerical values being up to 100% larger than the experimental values. It is very likely that the source of this error is the effect of the imperfect insulation on the bottom of the experimental apparatus. In addition, Wolff and Viskanta also noted that their temperature measurements were subject to scatter. The curves for y/H = 0.5 and 0.9 exhibit superior agreement to the experimental data as do results from [14] compared to those of [13] while the y/H = 0.1 curve deviates further.

The predicted solidification front locations from the present study are compared to experimental measurements from [12] and numerical predictions in the literature [13-15] in Fig. 5(b). The predictions from the present study are in acceptable agreement with the experimental results. The discrepancies in front locations at the start may be explained by the observations noted in [12] on the thermal inertia of the experimental apparatus as discussed above. At the later times, the predicted front location tends to lag behind the experimentally determined location. In addition, the numerical results fail to predict the increased thickness of the front at the bottom of the cavity. Both of these discrepancies may be attributed to the imperfect insulating material at the bottom of

the experimental apparatus [12]. There is clearly a need for more carefully controlled experiments against which to benchmark numerical simulations.

Results for Bridgman Growth of Succinonitrile

A different set of simulations were performed to simulate experiments on horizontal Bridgman crystal growth performed in related work [16]. Interface shapes and locations, temperature traces and melt velocities were measured in [16] in order to generate a database against which numerical simulations of solidification processes could be compared. The Bridgman growth process was described earlier with reference to Fig. 1(b).

The geometry and thermal boundary conditions are defined in Fig. 6. The origin of the z-coordinate is located at the mid-point of the adiabatic zone. The simulation domain extended from z = –19 mm in the solid to +40 mm in the liquid. Terrestrial gravity of $\boldsymbol{g}$ = 9.81 m/s^2 was applied. The material properties of pure succinonitrile as well as of borosilicate glass are listed in Table 6. As the result of a grid-independence study, a mesh of 177 × 24 uniform cells was employed (compared to 200 × 28 non-uniform cells reported in [16]). Two-dimensional simulations of the process have been found to be a good approximation for no-growth conditions but not so for growth conditions [16]. In the present study, both are modeled as being two-dimensional. Fully three-dimensional problems cannot presently be accommodated by the solution scheme, but this functionality is being added in ongoing work.

No-growth simulations

A case where the furnaces do not translate was considered first. In this instance, the solid/liquid interface forms in the gradient zone near z = 0 and does not move once steady state is attained. Figure 7 is a plot of the velocity vectors and isotherms for this case, both from the

enthalpy formulation [16] and the present front-tracking scheme. The dashed line is the interface location. A single, clockwise rotating longitudinal convective cell has formed in the SCN melt. Warm bulk fluid moves along the top wall and washes onto the top of the interface. The fluid then falls toward the bottom wall and is convected away. The interface takes on a distinctly curved shape with the solid being concave. This shape is due to the influence of convection on the interface shape; warm fluid introduced to the interface near the top wall acts to melt the interface back. As the fluid cools and falls towards the bottom wall the interface is distorted less. For the results from the present study shown in Fig. 7(b), the maximum convective velocity was found to be 1.32 mm/s at the location (y, z) of (–1.33, +1.00), which is near the interface where the applied temperature gradients are steepest. This value agrees well with the experimentally estimated value of 1.50 ± 0.08 mm/s in the same location and a predited value of 1.515 mm/s from [16]. As can be seen in Fig. 7, the results found from both simulations are in good agreement.

A comparison of interface shapes from the experiment and the two numerical schemes is shown in Fig. 8. The experimental data in this figure are from the middle vertical plane of the ampoule. In comparing the numerically calculated (present study) and measured interface shapes, the results agree to within a maximum discrepancy of 0.32 mm. This is acceptable agreement given the variability of the measured temperature boundary conditions (±1°C) and the experimental error of ±0.2 mm in determining the interface location. Other finite-volume, finite-element and finite-difference simulations of the same process [16, 23, 24] exhibit maximum discrepancies of 0.30 to 0.47 mm. Velocity and front location comparison results are summarized in Table 7.

Growth simulations

Bridgman growth at a 40 μm/s growth rate was investigated next. This is a more demanding problem since the thermal jackets translate at a steady velocity; hence, the solution becomes time-dependent. To simulate the movement of these jackets, the thermal boundary condition was translated at the same steady velocity (40 μm/s). A steady-state solution (with the boundary temperatures immobile) was used as the initial condition. The interface *shape* eventually reaches a steady profile and the interface as a whole is pulled along by the boundary temperatures moving at 40 μm/s after t = 300 s.

Velocity vectors and isotherms for this case are shown in Fig. 9, with the simulated results from [16] plotted in Fig. 9(a) and results from the present study in Fig. 9(b). Warm bulk fluid moves along the top wall and washes on to the top of the interface. The fluid then falls toward the bottom wall and is convected away. The interface takes on a distinctly curved shape with the solid being concave, as in the no-growth simulations, with the distortion in interface shape being greater in the growth case.

Interface shapes for this 40 μm/s growth case are shown in Fig. 10. The experimental data are from [3] and [16]. Again, the numerically determined interface shape agrees well with the experiments, as well as with the predictions from [16]. The present numerical predictions show better agreement with the experimental front locations and shape than those from [16]. This is not surprising since an explicit front tracking approach is expected to be more successful at predicting interface information when compared to interface-capturing methods such as the enthalpy method employed in [16]. Selected velocity and front location results for this case are compared in Table 8.

CONCLUSIONS

A fixed-grid front-tracking algorithm for the simulation of directional solidification with melt convection has been developed. The front-tracking scheme, previously formulated in Part I of this work for conduction-only phase-change problems [11], has been extended so that a solution scheme for solving convective velocities in the melt is included. This required special adaptations to the discrete forms of convective and diffusive fluxes employed in the finite-volume SIMPLE algorithm [17, 18].

The performance of this extended algorithm was then examined by simulating the directional solidification of pure tin, and comparing the results to experimental data [12] and computer simulations [13-15] available in the literature. The numerical results found using the front-tracking approach were found to agree reasonably well with the experimental data, in terms of interface shapes and temperature traces. Additionally, the results exhibited similar good agreement with results from other simulations in the literature. Computational costs for the current scheme were comparable to simpler, single-domain approaches that do not explicitly track the interface.

The horizontal Bridgman growth of pure succinonitrile was also simulated. Both a no-growth and a growth (at 40 μm/s) case were considered. The results were compared with experimentally measured interface shape and melt velocity data. It was observed that the agreement between the numerical and experimental results was good. The interface shapes calculated using the front-tracking algorithm exhibited superior agreement with the experiments than those calculated using a single-domain approach that does not explicitly track the front. Complex, time-dependent velocity, interface shapes and temperature fields were resolved by the algorithm, giving insight into the role of convection on Bridgman growth

The results shown in this paper demonstrate that this front-tracking scheme is an accurate

yet highly computationally efficient means of solving directional solidification problems with melt convection. In ongoing work, the fixed-grid front-tracking scheme described in the present study is being extended to handle three-dimensional, alloy solidification problems.

REFERENCES

1. Flemings, M. C., *Solidification Processing* (McGraw-Hill, 1974).
2. Kou, S., *Transport Phenomena and Materials Processing* (John Wiley & Sons, Inc., New York, 1996).
3. de Groh III, H. C. and Lindstrom, T., Interface shape and convection during solidification and melting of succinonitrile, *NASA Tech Memo. 106487*, June 1994.
4. Garimella, S. V., McNulty, J. P. and Schlitz, L. Z., Formation and suppression of channels during upward solidification of a binary mixture, *Metall. and Mater. Trans. A,* **26A**, 971 (1995).
5. Magirl, C. S. and Incropera, F. P., Flow and morphological conditions associated with unidirectional solidification of aqueous ammonium chloride, *J. Heat Transfer*, **115**, 1036 (1993).
6. Hellawell, A., Sarazin, J. R. and Stuebe, R. S., Channel convection in partly solidified systems, *Phil. Trans. R. Soc. London,* **345A**, 507 (1993).
7. Copley, S. M., Giamei, A. F., Johnson, S. M. and Hornbecker, M. F., The origin of freckles in unidirectionally solidified castings, *Met. Trans.,* **1**, 2193 (1970).
8. de Cheveigné, S., Guthmann, C., and Lebrun, M.-M., Nature of the transition of the solidification front of a binary mixture from a planar to a cellular morphology, *J. Crystal Growth*, **73**, 242 (1985).
9. Eshelman, M. A., Seetharaman, V. and Trivedi, R., Cellular spacings—I. Steady-state growth, *Acta Met.,* **36**, 1165 (1988).
10. Labonia, G., Timchenko, V., Simpson, J. E., Garimella, S. V., Leonardi, E. and de Vahl Davis, G., Reconstruction and advection of a moving interface in three dimensions on a fixed grid,

Num. Heat Transfer, **34**, 121 (1998).

11. Li, C. Y., Garimella, S. V. and Simpson, J. E., A fixed-grid front-tracking algorithm for solidification problems. Part I - Method and Validation, *Num. Heat Transfer* (in press).
12. Wolff, F., and Viskanta, R., Solidification of a pure metal at a vertical wall in the presence of liquid superheat, *Int. J. Heat Mass Transfer*, **31**, 1735 (1988).
13. Raw, W. Y. and Lee, S. L., Application of weighting function scheme on convection-conduction phase change problems, *Int. J. Heat Mass Transfer*, **34**, 1503 (1991).
14. Simpson, J. E. and Garimella, S. V., An investigation of solutal, thermal and flow fields in unidirectional alloy solidification, *Int. J. Heat Mass Transfer*, **41**, 2485 (1998).
15. Zhang, H., Prasad, V., and Moallemi, M . K., Numerical algorithm using multizone adaptive grid generation for multiphase transport processes with moving and free boundaries, *Num. Heat Transfer*, **29B**, 399 (1996).
16. Simpson, J. E., Garimella, S. V. and de Groh III, H. C., An experimental and numerical investigation of the Bridgman growth of succinonitrile, *AIAA J. Thermophysics and Heat Transfer*, **16**, 324 (2002).
17. Patankar, S. V. and Spalding, D. B., A calculation procedure for heat, mass and momentum transfer in three-dimensional parabolic flow, *Int. J. Heat and Mass Transfer*, **15**, 1787 (1972).
18. Patankar, S. V., *Numerical Heat Transfer and Fluid Flow* (Hemisphere Publishing Corp., 1980).
19. Hedges, E. S., *Tin and Its Alloys* (Edward Arnold, London, 1960).
20. Cubberly, W. H., *Metals Handbook, Properties and Selection: Nonferrous Alloys and Pure Metals*, 9th Edn. (ASM. Metal Park, Ohio, 1979).
21. de Vahl Davis, G., Natural convection of air in a square cavity: A benchmark solution, *Int. J.*

Num. Meth. Fluids, **3**, 249 (1983).

22. Özişik, M. N., *Heat Conduction* (John Wiley, 1980).
23. de Groh III, H. C. and Yao, M. Numerical and experimental study of transport phenomena in directional solidification of succinonitrile, *Transport Phenomena in Solidification*, HTD- Vol. 284, ASME, New York (1994).
24. Yeoh, G. H., de Vahl Davis, G., Leonardi, E., de Groh III, H. C. and Yao, M., A numerical and experimental study of natural convection and interface shape in crystal growth, *J. Crystal Growth*, **173**, 492 (1997).
25. Paradies, C. J., The Influence of Forced Convection during Solidification on Fragmentation of the Mushy Zone of a Casting, Ph.D. Dissertation, Rensselaer Polytechnic Institute (1993).

NOMENCLATURE

A	area
$a_{i,j}$	coefficients in pressure correction equations
B_K^{ϕ}	convective coefficients in discrete equations
$b_{i,j}$	source term in pressure correction equation
c_p	specific heat capacity at constant pressure
D_K^{ϕ}	diffusive coefficients in discrete equations
dl_k	control length
g	gravity
H	height of computational domain (Fig. 1)
k	thermal conductivity
L	length
n	ordinate in normal direction
P	pressure
P'	pressure correction
S	source term in governing equations
t	time
T	temperature
U	velocity
V	front moving velocity
x, y	Cartesian coordinates

Greek

α	thermal diffusivity
β_T	thermal expansion coefficient
ε	tolerance
ΔH	Enthalpy of freezing
Δt	time step
Δx, Δy	spatial mesh sizes
ϕ	nondimensional temperature, $(T-T_C)/(T_H-T_C)$
Θ	nondimensional temperature, $(T_m-T_C)/(T_H-T_C)$
Φ	general variable for governing equations, (temperature or velocity)
μ	viscosity
ρ	density
τ	ordinate in tangential direction
ν	kinematic viscosity

Subscripts

0	initial condition
E	east node
e	east control surface
I,J (*i,j*)	indices of grid (staggered) locations in *x* and *y* directions
l	liquid
m	at solidification front

nb	neighbor points
N	north node
n	north control surface
P	grid node
S	south node
s	south control surface
s	solid
T	thermal
W	west node
w	west control surface

Superscripts

~	vector
0	initial guess
n	time step

FIGURE CAPTIONS

Fig. 1 (a) The computational domain and boundary conditions for the solidification of pure tin. This domain is identical to that used for the experimental investigation reported in [12]. H/L = 0.75, T_H = 233°C, T_C = 229°C, and T_m = 231.9°C. (b) Schematic of horizontal Bridgman crystal growth process.

Fig. 2 (a) Illustration of arrangement of the interface and marker points in 2-D and enlarged detail of cut cell with marker point and intersection point. (b) Different types of intersection of a finite volume cell by the interface.

Fig. 3 (a) Control volume cell intersected by the interface with intersection point and marker points. (b) Illustration of pressure correction for a cell intersected by the interface.

Fig. 4 Velocity vectors and isotherms for the directional solidification of pure tin. Isotherms are at intervals of $\Delta\theta = 0.1$ in the solid region and $\Delta\theta = 0.02$ in the melt. Bold line is the front location: (a) t = 0.165 h, (b) t = 0.569 h and (c) t = 1.896 h.

Fig. 5 Comparison of experimentally determined [12] and numerically predicted results. (a) temperatures in the melt region at t = 0.077 h and (b) front location at various times. Note that no front locations are provided in [15] for t = 1.896 h.

Fig. 6 The computational domain and applied thermal boundary conditions along the exterior of the top and bottom ampoule walls. These boundary conditions are from experimental measurements in [16].

Fig. 7 Velocity vectors and isotherms for the directional solidification of pure SCN under no-growth conditions: (a) simulations presented in [16] and (b) simulations from present study. Dashed lines represent the front location.

Fig. 8 Comparison of interface shapes for the SCN no-growth case.

Fig. 9 Velocity vectors and isotherms for the directional solidification of pure SCN under 40 μm/s growth conditions after t = 300 s (a) results from simulations in [16] (b) results from the present study. Dashed lines represent the front location.

Fig. 10 Comparison of numerically determined and experimentally measured interface shapes for the 40 μm/s growth case.

Table 1. Coefficients for the discretized pressure correction equation (Eq. 13).

$a_{I+1,J}$	$a_{I-1,J}$	$a_{I,J+1}$	$a_{I,J-1}$	$b'_{I,J}$
$\frac{dt}{a_{i,J}}$	$\frac{dt}{a_{i-1,J}}$	$\frac{dt}{a_{I,j}}$	$\frac{dt}{a_{I,j-1}}$	$U^*_{i-1,J} \cdot dy - U^*_{i,J} \cdot dy + V^*_{I,j-1} \cdot dx - V^*_{I,j} \cdot dx$

Table 2. New coefficients for the discretised pressure correction equation for cut cells.

$a_{I+1,J}$	$a_{I-1,J}$	$a_{I,J+1}$	$a_{I,J-1}$	$b'_{I,J}$
$\frac{dt}{a_{i,J} \cdot dx} \cdot \overline{CD}$	$\frac{dt}{a_{i-1,J} \cdot dx} \cdot \overline{AB}$	$\frac{dt}{a_{I,j} \cdot dy} \cdot \overline{BC}$	0	$U^*_{i-1,J} \cdot \overline{AB} - U^*_{i,J} \cdot \overline{CD} + -V^*_{I,j} \cdot \overline{BC}$

Table 3. Thermophysical properties for tin [19, 20].

	Property	Value	Unit
Tin (liquid)	k_l	32.6	W/mK
	c_{pl}	255	J/kgK
	ρ	7300	kg/m^3
	ΔH	5.94×10^{4}	J/kg
	μ	3.77×10^{-3}	Ns/m
	β_T	1.06×10^{-4}	1/K
Tin (solid)	k_s	56.5	W/mK
	c_{ps}	255	J/kgK
	ρ	7300	kg/m^3
	T_m	231.9	°C

Table 4. Effect of grid size on the results for unidirectional solidification of pure tin.

($\Delta t = 6.250 \times 10^{-6}$)

Grid	h	u_{max}	v_{max}	θ_{mid}	x_f
500 time steps					
21 × 16	0.04	0.5457 (0.5, 0.05) 37.39%	0.4485 (0.05, 0.4) 17.90%	0.7476 2.38%	0.7921 3.12%
41 × 31	0.02	0.3516 (0.375, 0.65) 11.48%	0.3492 (0.075, 0.4) 8.20%	0.7556 1.33%	0.7723 0.55%
61 × 46	0.015	0.3825 (0.4167, 0.65) 3.70%	0.3724 (0.0833, 0.41167) 2.13%	0.7605 0.69%	0.7699 0.23%
81 × 61	0.01	0.3972 (0.4375, 0.0625)	0.3805 (0.075, 0.4)	0.7658	0.7681
20,000 time steps					
21 × 16	0.04	0.3055 (0.25, 0.55) 28.50%	0.3122 (0.05, 0.3) 29.9%	0.5236 6.85%	0.4050 1081%
41 × 31	0.02	0.3792 (0.1, 0.55) 11.26%	0.3958 (0.025, 0.425) 11.14%	0.5278 6.1%	0.4240 6.63%
61 × 46	0.015	0.4127 (0.2333, 0.3833) 3.42%	0.4246 (0.0883, 0.5167) 4.67%	0.5542 1.40%	0.4473 1.5%
81 × 61	0.01	0.4273 (0.2545, 0.3625)	0.4454 (0.075, 0.5125)	0.5621	0.4541

Table 5. Effect of time-step size on the results for unidirectional solidification of pure tin. (61 × 46 mesh)

Nondimensional finish time = 0.03375				
Δt (steps)	u_{max}	v_{max}	θ_{mid}	x_f
6.25×10^{-5} (500)	0.4952 (0.325, 0.65) 0.4%	0.4608 (0.1,0.475) 2.52%	0.7170 0.51%	0.5902 0.1%
3.125×10^{-5} (1,000)	0.4957 (0.325, 0.675) 0.3%	0.4713 0.3%	0.7278 0.03%	0.5917 0.0%
1.25×10^{-5} (2,500)	0.4966 0.12%	0.4725 0.04%	0.7279 0.01%	0.5920 0.0%
0.625×10^{-5} (5,000)	0.4972	0.4727	0.7280	0.5923
Nondimensional finish time = 0.135				
6.25×10^{-5} (2,000)	0.3687 (0.1, 0.55) 0.49%	0.4029 (0.25, 0.425) 1.54%	0.5069 3.0%	0.4036 0.35%
3.125×10^{-5} (4,000)	0.3675 0.16%	0.4049 1.05%	0.5007 1.75%	0.4029 0.17%
1.25×10^{-5} (10,000)	0.3670 0.03%	0.4076 0.39%	0.4934 0.26%	0.4026 0.12%
0.625×10^{-5} (20,000)	0.3669	0.4092	0.4921	0.4022

Table 6. Thermophysical properties for SCN [25] and the borosilicate glass ampoule [23].

	Property	Value	Units
SCN (liquid)	k_l	0.223	W/mK
	c_{pl}	2000	J/kgK
	ρ	990	kg/m^3
	ΔH	46.24	J/kg
	μ	3.0×10^{-3}	Ns/m
	β_T	8.1×10^{-4}	1/K
SCN (solid)	k_s	0.225	W/mK
	c_{ps}	1955	J/kgK
	ρ	990	kg/m^3
	T_m	58.08	°C
Borosilicate glass	k_w	1.2	W/mK
	c_{pw}	753.5	J/kgK
	ρ_w	2300	kg/m^3

Table 7. Comparison between experimental data [16] and computed results (present study and [16]), for the no-growth case in SCN Bridgman crystal growth.

	Experimental data [16]	**Numerical results [16]**	**Present study**
Average deviation of front locations		0.20 (mm)	0.15 (mm)
Maximum deviation of front locations		0.35 (mm)	0.32 (mm)
Maximum velocity (y,z)	1.50 (mm/s) (-1.30,+0.90)	1.515 (mm/s) (-1.30,+0.90)	1.32 (mm/s) (-1.33,+1.00)

Table 8. Comparison between experimental data [16] and computed results (present study and [16]) under growth (40μm/s) conditions for SCN Bridgman crystal growth.

	Numerical results [16]	**Numerical results (Present study)**
Averaged deviation of front locations	0.23 (mm)	0.21 (mm)
Maximum-deviation of front locations	1.22 (mm)	0.43(mm)

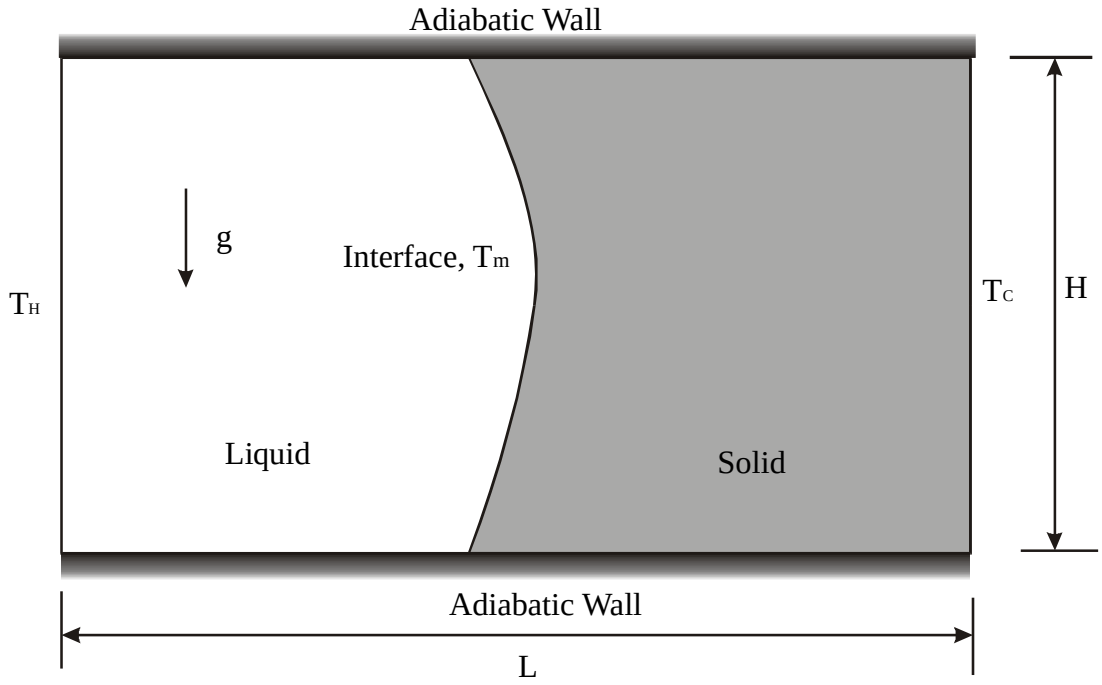

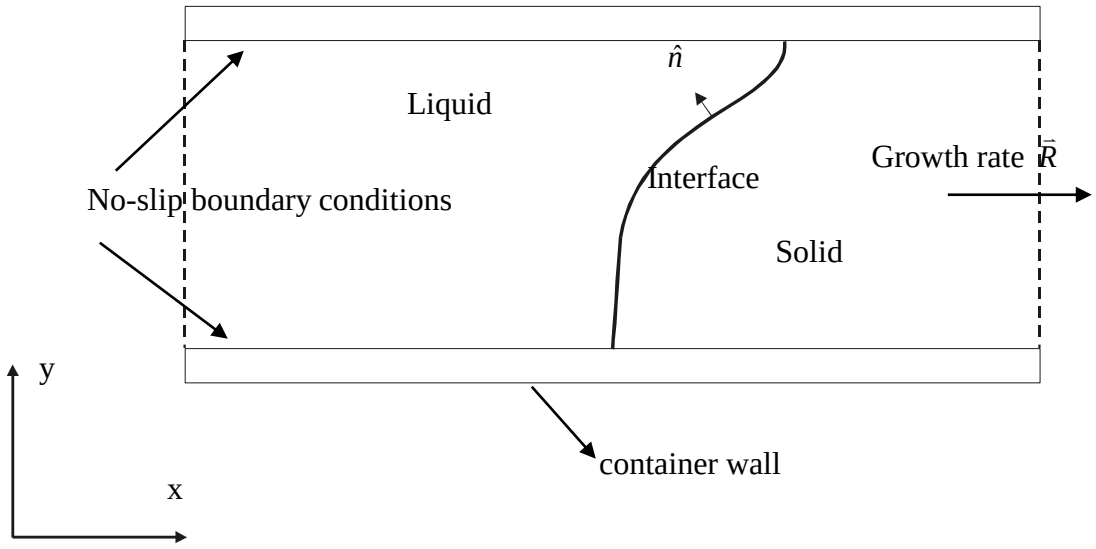

Figure 1, Li et al.

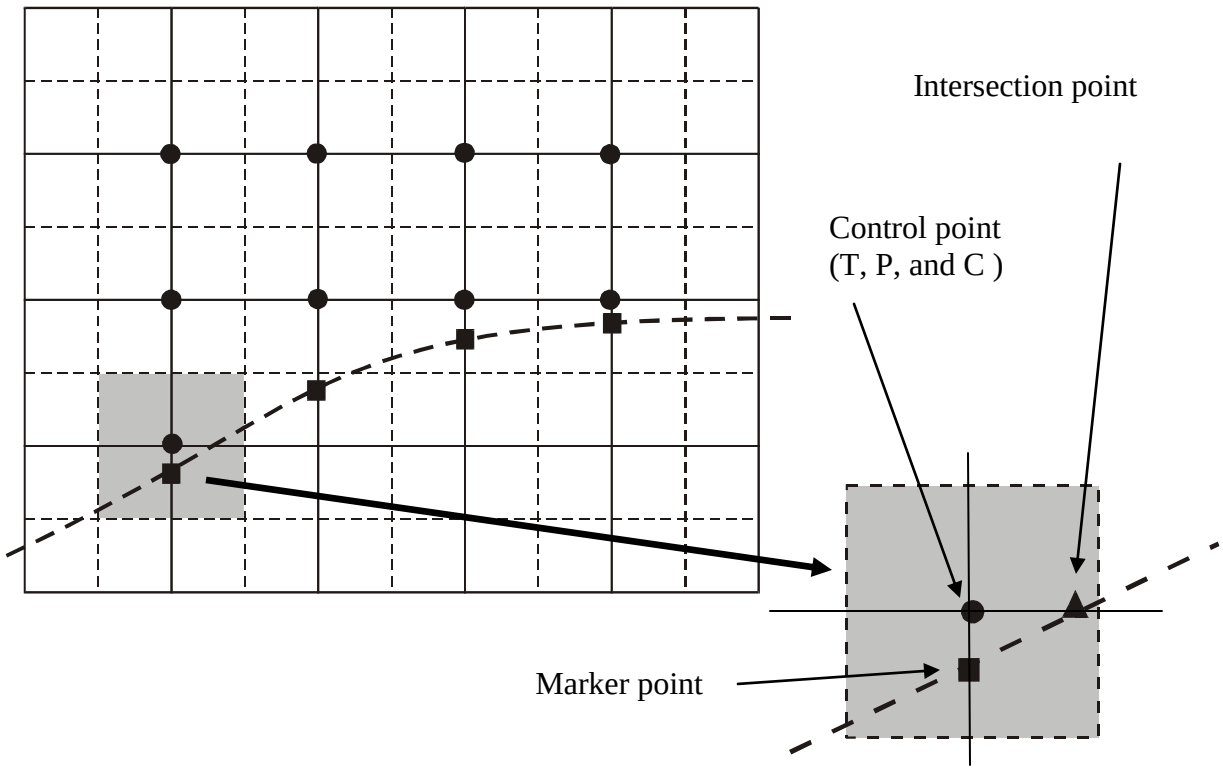

(a)

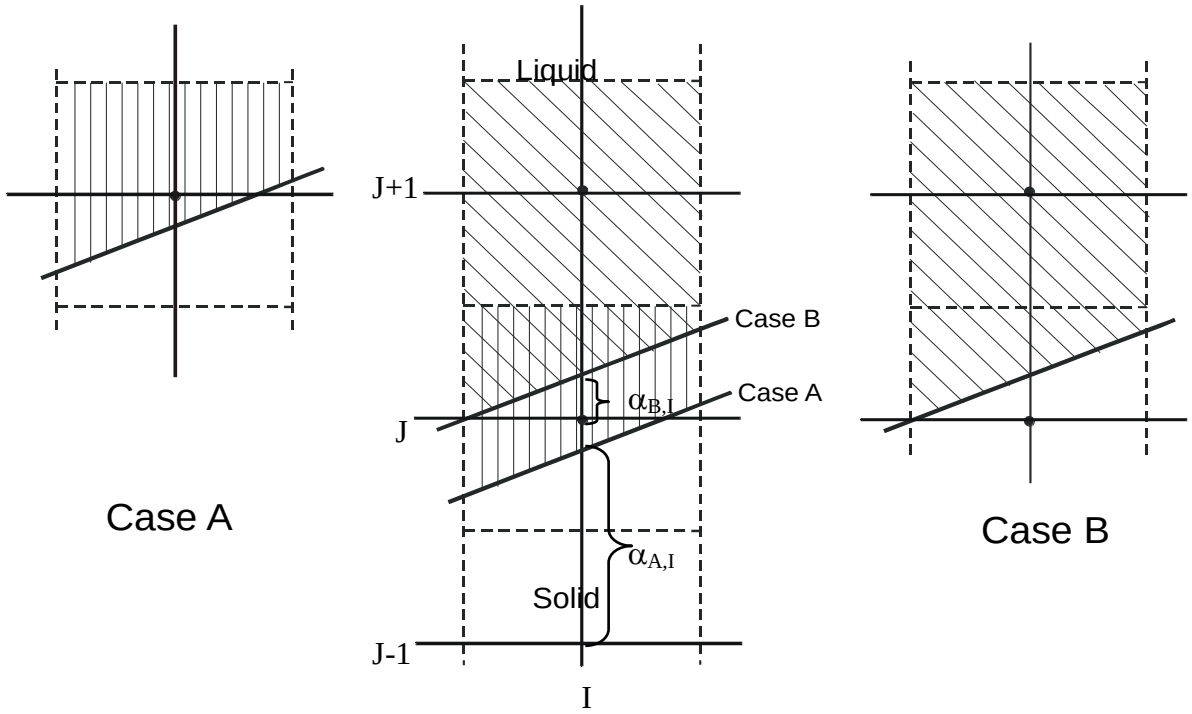

(b)

Figure 2, Li et al.

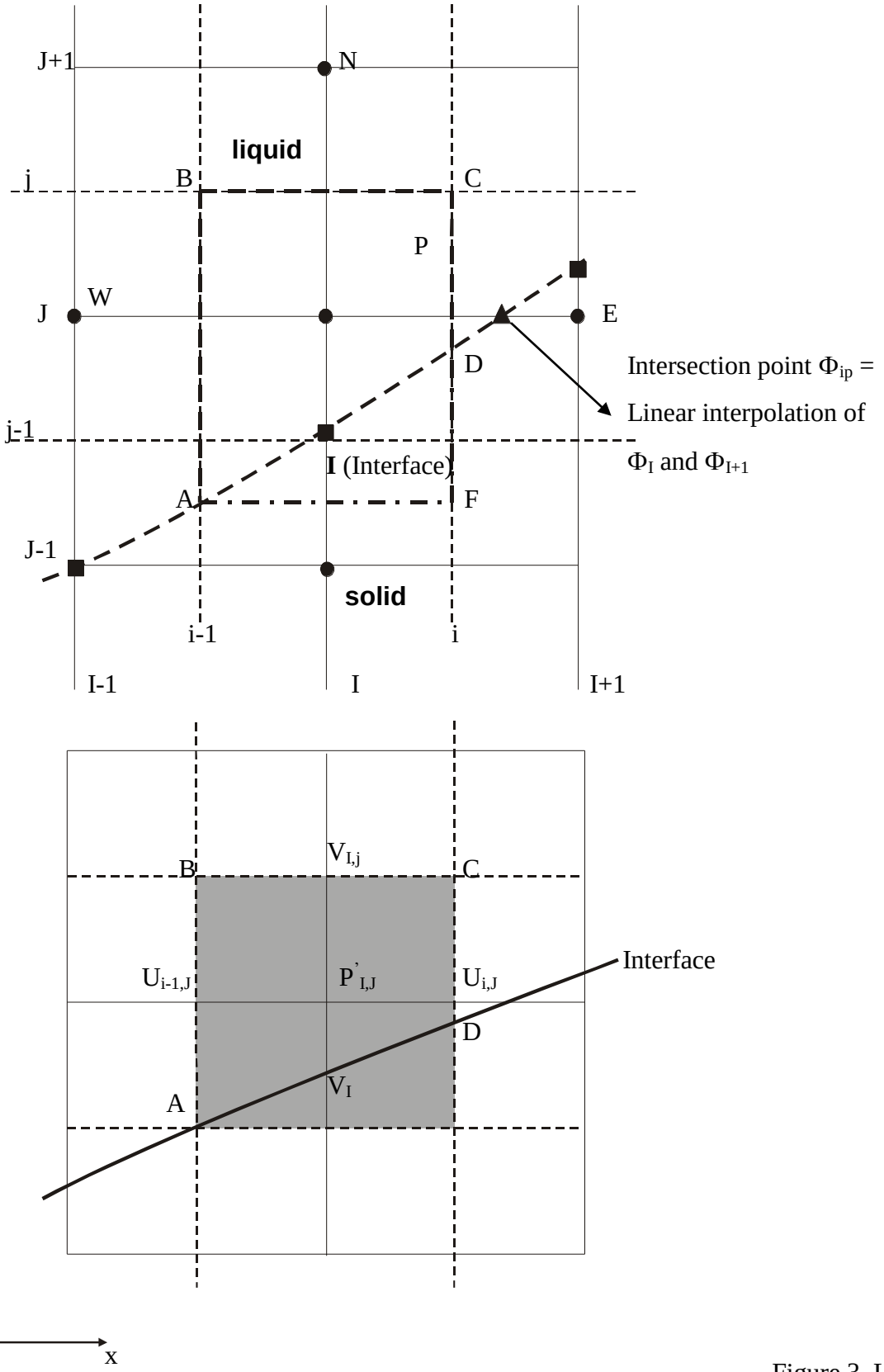

Figure 3, Li et al.

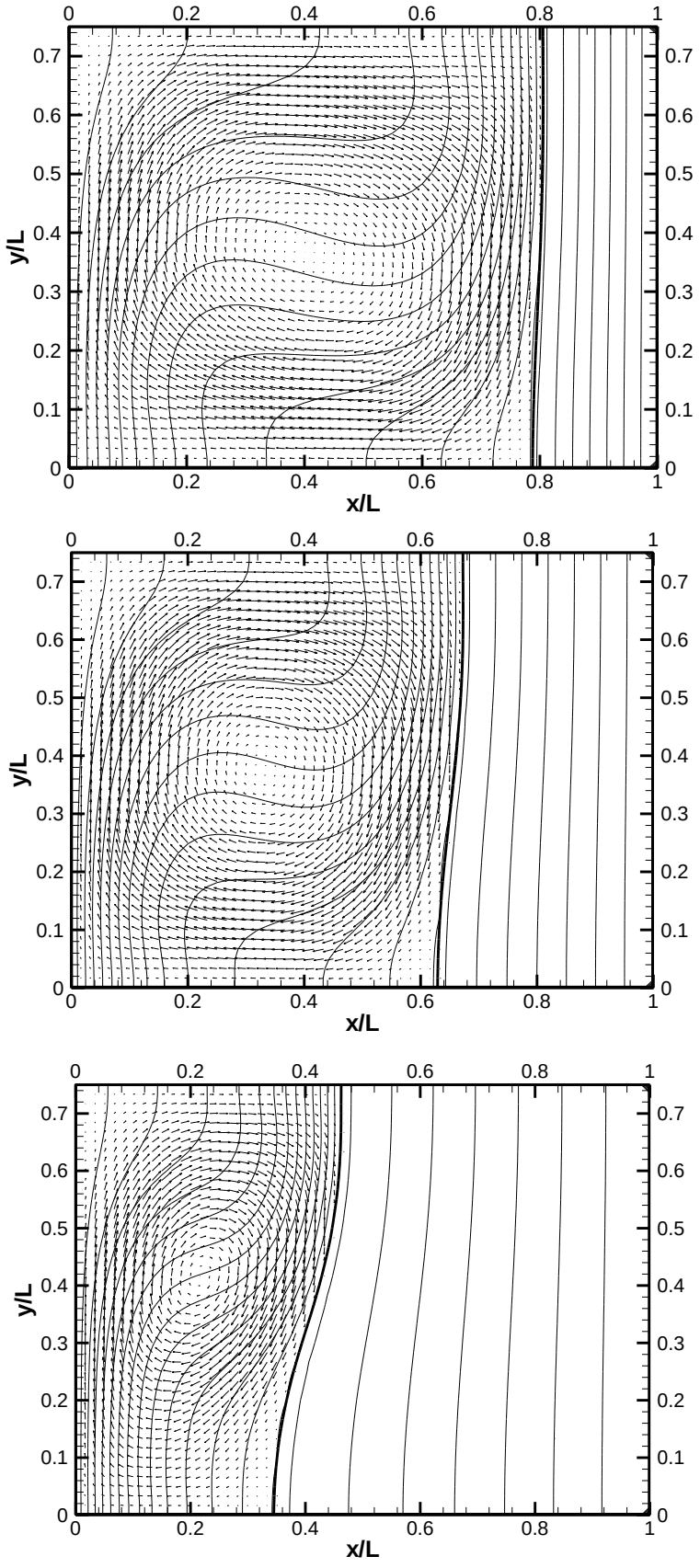

Figure 4, Li et al.

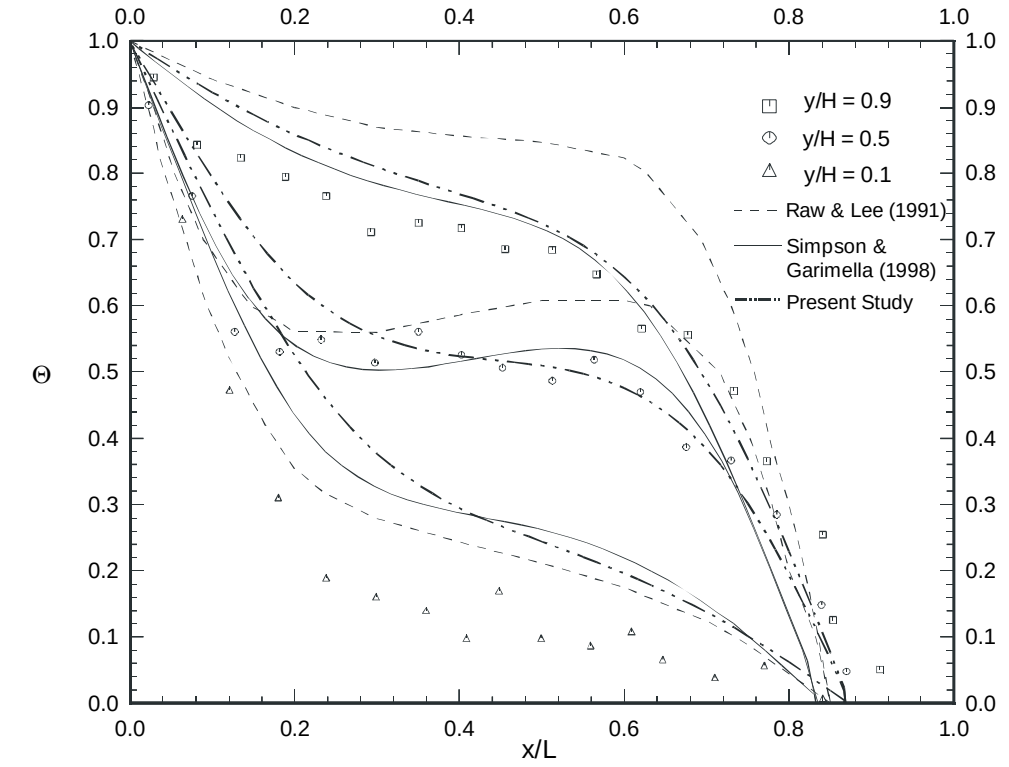

(a)

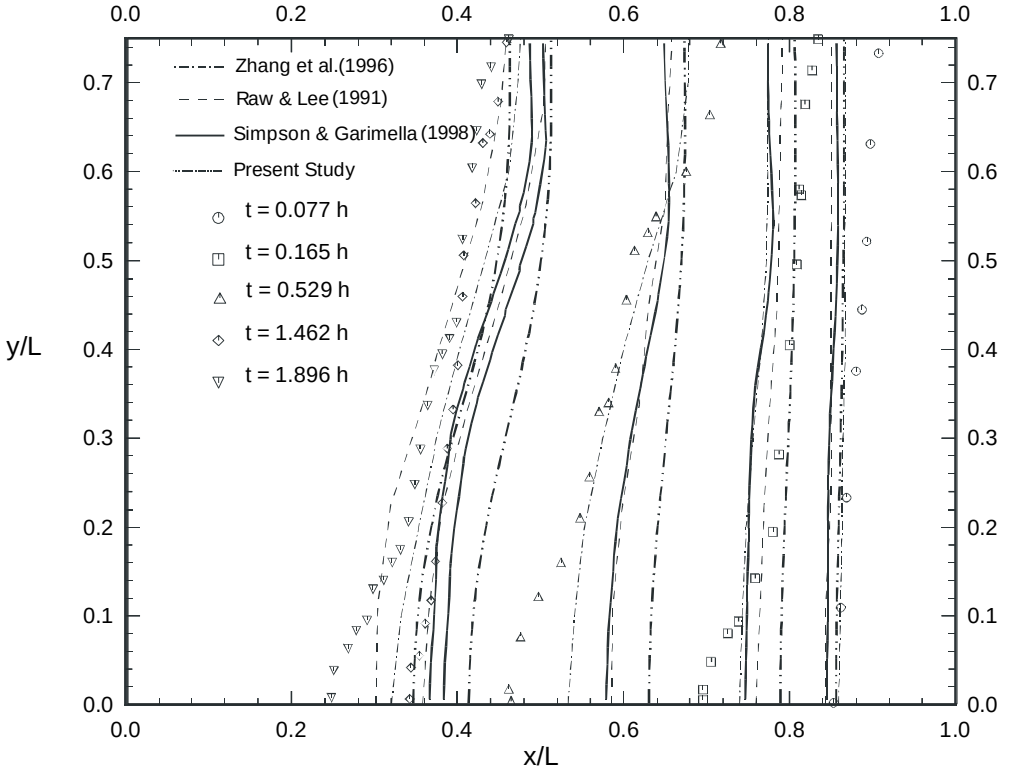

(b)

Figure 5, Li et al.

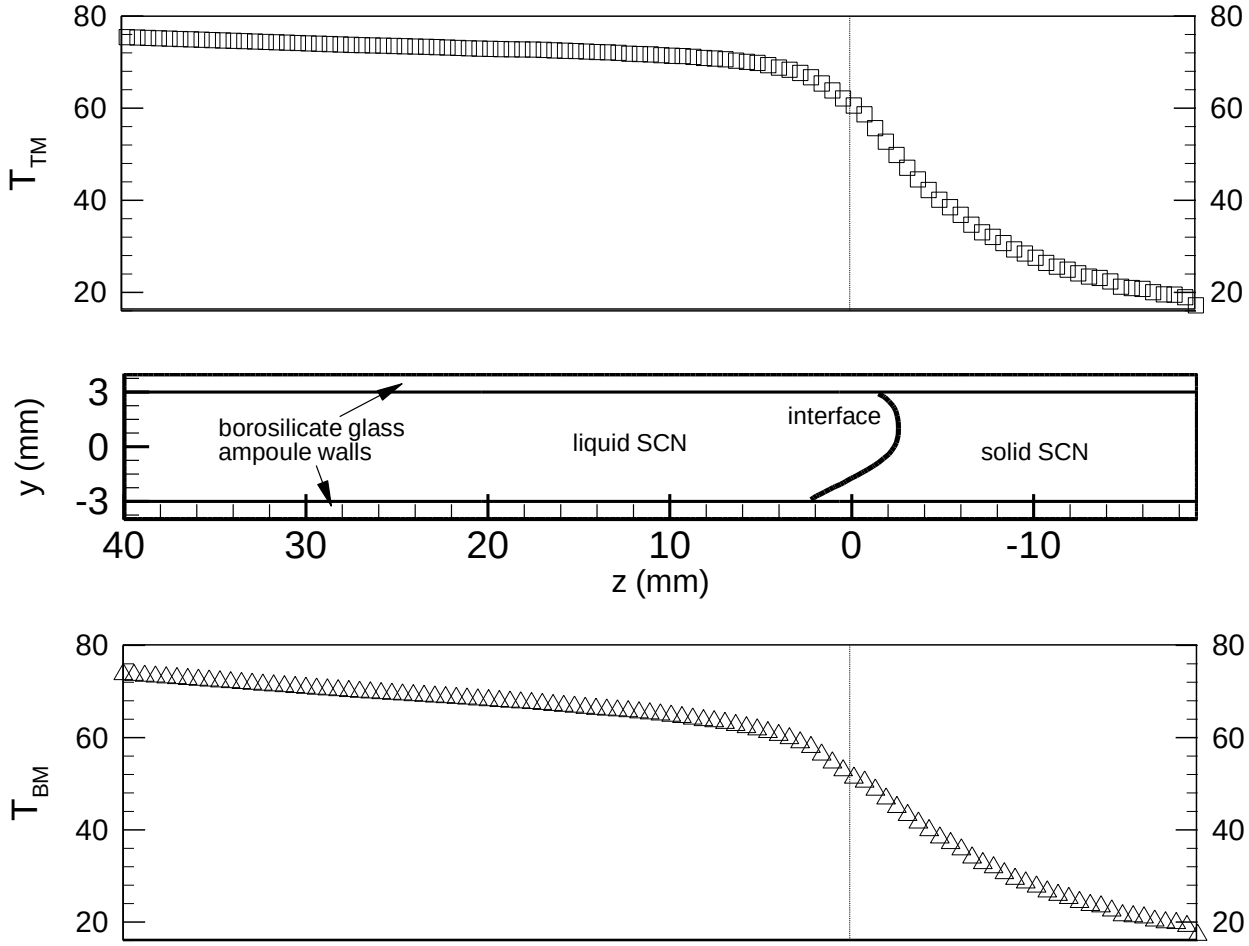

Figure 6, Li et al.

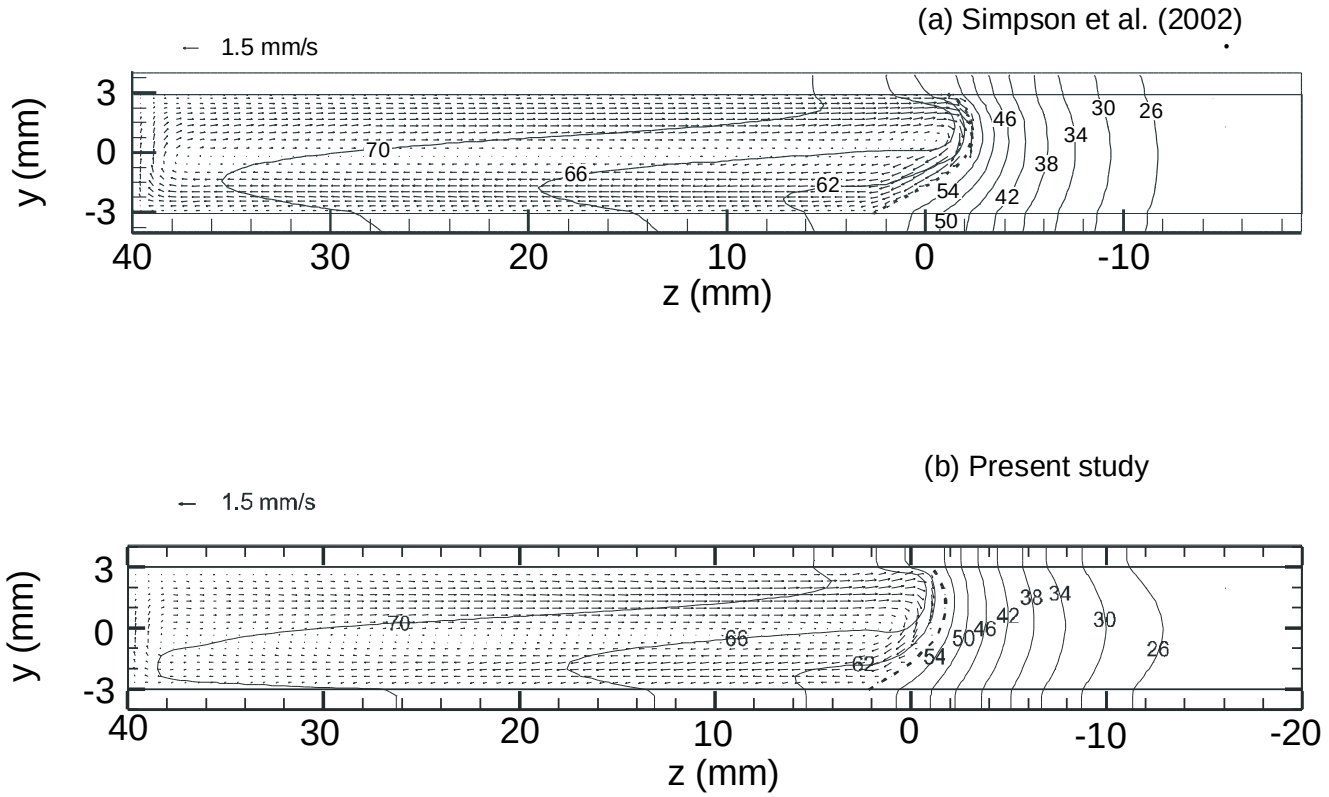

Figure 7, Li et al.

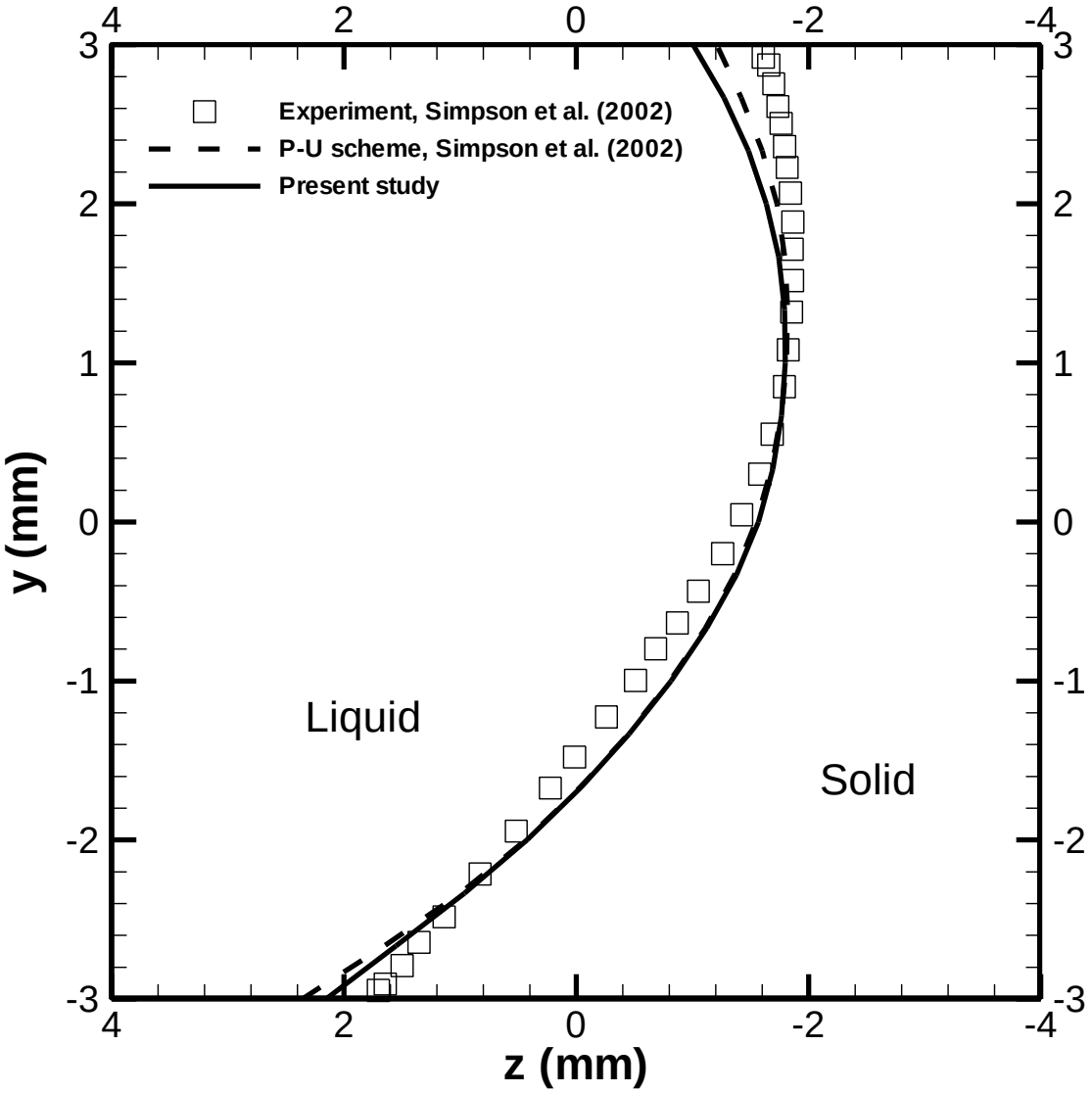

Figure 8, Li et al.

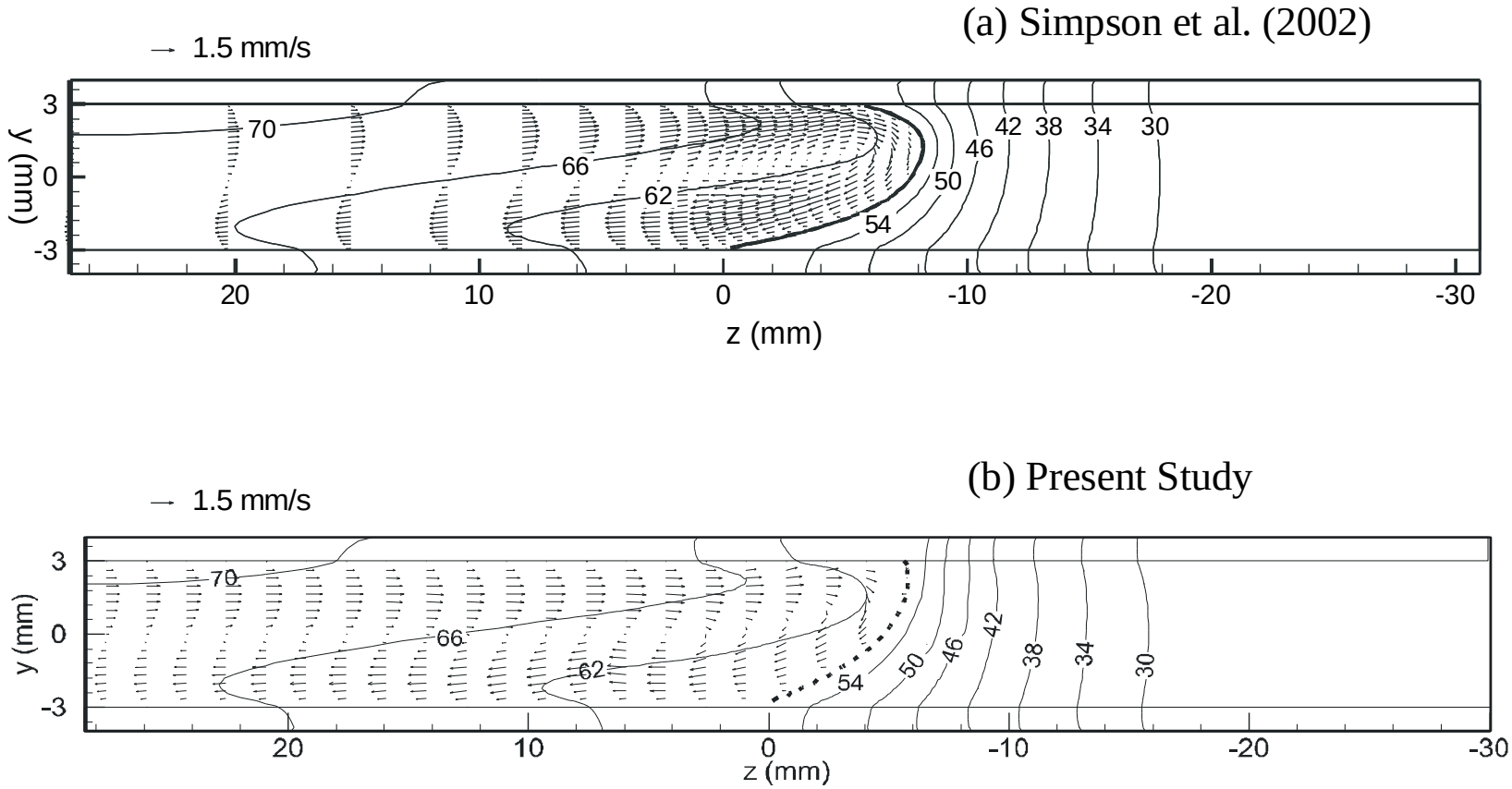

Figure 9, Li et al.

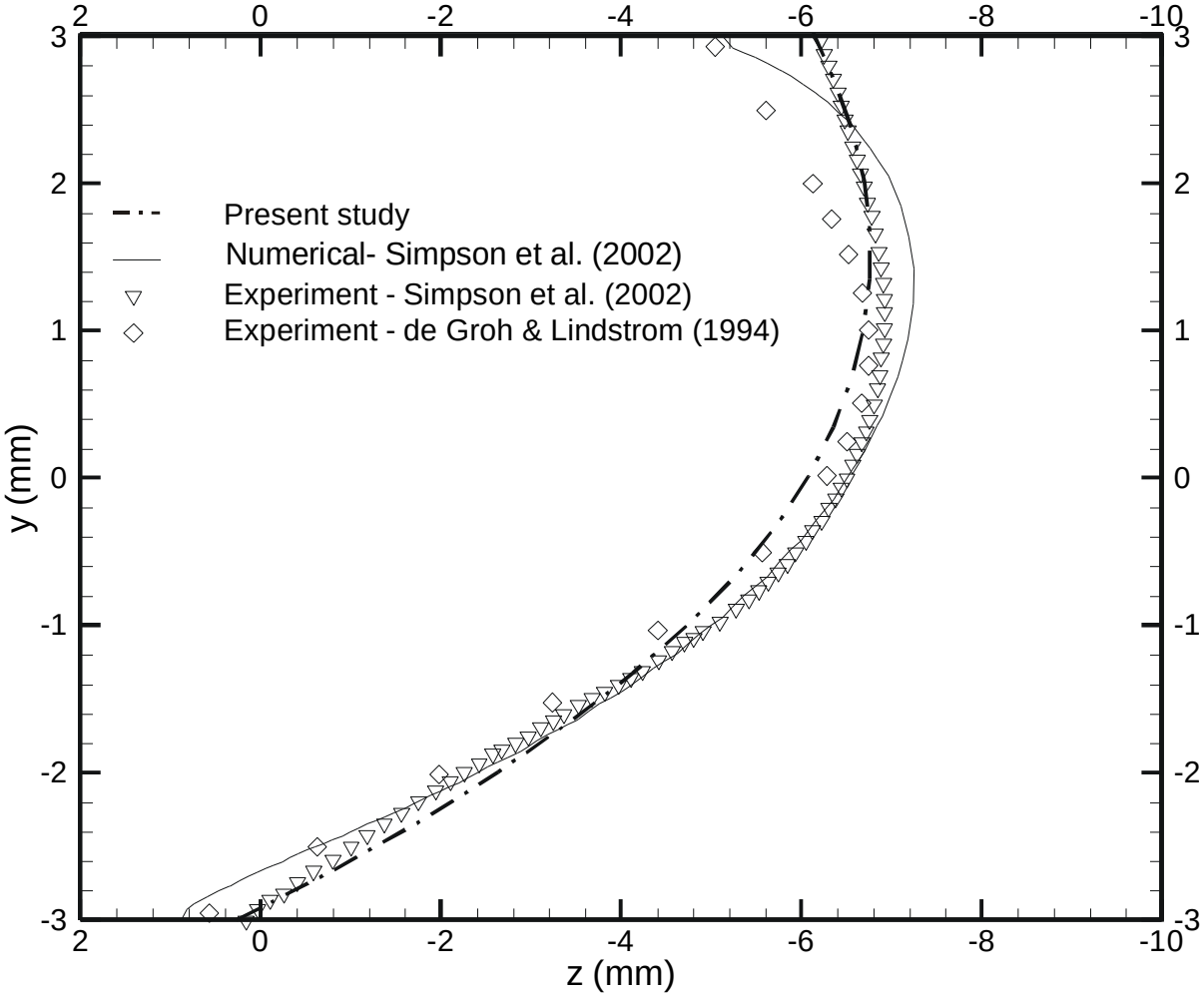

Figure 10, Li et al.